

Impact of inherent energy barrier on spin-orbit torques in magnetic-metal/semimetal heterojunctions

Tenghua Gao^{a,1,2,3} Alireza Qaiumzadeh^{a,4} Roberto E. Troncoso^{a,4,5}
Satoshi Haku,² Hongyu An,⁶ Hiroki Nakayama,² Yuya Tazaki,² Song
Zhang,³ Rong Tu,³ Akio Asami,² Arne Brataas,⁴ and Kazuya Ando^{b2,1,7}

¹*Keio Institute of Pure and Applied Science,
Keio University, Yokohama 223-8522, Japan*

²*Department of Applied Physics and Physico-Informatics,
Keio University, Yokohama 223-8522, Japan*

³*State Key Laboratory of Advanced Technology for Materials Synthesis and Processing,
Wuhan University of Technology, Wuhan, China*

⁴*Center for Quantum Spintronics, Department of Physics,
Norwegian University of Science and Technology, NO-7491 Trondheim, Norway*

⁵*School of Engineering and Sciences,
Universidad Adolfo Ibáñez, Santiago, Chile*

⁶*College of New Materials and New Energies,
Shenzhen Technology University, Shenzhen 518118, China*

⁷*Center for Spintronics Research Network,
Keio University, Yokohama 223-8522, Japan*

^a These authors contributed equally

^b Correspondence and requests for materials should be addressed to ando@appi.keio.ac.jp

Abstract

Spintronic devices are based on heterojunctions of two materials with different magnetic and electronic properties. Although an energy barrier is naturally formed even at the interface of metallic heterojunctions, its impact on spin transport has been overlooked. Here, using diffusive spin Hall currents, we provide evidence that the inherent energy barrier governs the spin transport even in metallic systems. We find a sizable field-like torque, much larger than the damping-like counterpart, in $\text{Ni}_{81}\text{Fe}_{19}/\text{Bi}_{0.1}\text{Sb}_{0.9}$ bilayers. This is a distinct signature of barrier-mediated spin-orbit torques, which is consistent with our theory that predicts a strong modification of the spin mixing conductance induced by the energy barrier. Our results suggest that the spin mixing conductance and the corresponding spin-orbit torques are strongly altered by minimizing the work function difference in the heterostructure. These findings provide a new mechanism to control spin transport and spin torque phenomena by interfacial engineering of metallic heterostructures.

Introduction

Junctions formed at the contact between two different materials are fundamental building blocks of solid-state devices. Prominent examples include junctions consisting of two materials with different electronic properties, such as metal/semiconductor junctions. When a metal is brought into contact with a semiconductor, a potential barrier for electrons is formed, as shown in Fig. 1a, due to the mismatch of the work functions of the two materials [1, 2]. Since the energy barrier, known as a Schottky barrier, governs charge transport across the interface, energy barrier engineering plays a key role in improving the performance of electronic devices in a variety of modern electronic applications [3].

An alternative technology that exploits the electron spin rather than its charge, spintronics, relies on junctions consisting of two materials with different magnetic properties [4, 5]. Emerging spin-orbitronic technology is based on the ability to manipulate the magnetization in magnetic/nonmagnetic-material junctions through bulk and interfacial spin-orbit couplings [6]. In a magnetic heterostructure, a charge current applied parallel to the interface generates a nonequilibrium spin current and spin polarization via the spin Hall effect due to the bulk spin-orbit coupling in the heavy metal layer [7] and/or

the Rashba-Edelstein effect due to the spin-orbit coupling at the interface [8–10]. The nonequilibrium spins arising from the spin-orbit coupling exert spin-orbit torques (SOTs) on the spins in the ferromagnetic layer, enabling electrical manipulation of the magnetization. Manipulation of magnetization by SOTs, including field-like (FL) and damping-like (DL) torques, is responsible for the development of many ultralow-power and fast spin-orbitronic nanodevices based on spin-orbit coupling, such as nonvolatile magnetic memories [11], nanoscale microwave or terahertz sources [12, 13], and neuromorphic computing devices [14].

Analogous to metal/semiconductor junctions, energy barriers are ubiquitous in solid-state devices, including spin-orbitronic devices. Even in a metal/metal heterojunction, a difference in the work functions of the two adjacent layers results in the formation of an energy barrier, manifested by a contact potential difference. This suggests that interface engineering of metallic heterostructures may provide a route to control and improve the performance of spin-orbitronic devices because the SOTs originating from the bulk spin Hall effect are governed by spin transport across the interface [15, 16]. Although the impact of an insertion layer on spin transport and SOTs has been investigated extensively [17–22], the role of inherent barriers in metallic spin-orbitronic devices has been overlooked.

In this work, we report the observation of SOTs governed by energy barriers inherent at metallic interfaces. By measuring SOTs for $\text{Ni}_{81}\text{Fe}_{19}/\text{Bi}_{0.1}\text{Sb}_{0.9}$ bilayers without any insertion layer, we find that the spin Hall effect in the semimetal $\text{Bi}_{0.1}\text{Sb}_{0.9}$ layer generates a sizable FL torque, which is several times larger than the induced DL torque, in sharp contrast to the conventional SOTs originating from the bulk spin Hall effect in metallic heterostructures. Our observation shows a counterintuitive larger imaginary part $\text{Im}[G^{\uparrow\downarrow}]$ relative to the real part $\text{Re}[G^{\uparrow\downarrow}]$ of the spin mixing conductance in the $\text{Ni}_{81}\text{Fe}_{19}/\text{Bi}_{0.1}\text{Sb}_{0.9}$ bilayers, which is consistent with our theory. The theory reveals that spin-dependent hopping and spin-independent hopping determine the spin mixing conductance, which characterizes the spin transmission and reflection, and hence DL and FL torques in ferromagnetic-metal/semimetal junctions. By replacing the $\text{Ni}_{81}\text{Fe}_{19}$ layer with $\text{Co}_{72}\text{Tb}_{28}$ to minimize the size of the energy barrier, we show that spin transmission across the interface becomes more efficient, as evidenced by a more than two orders of magnitude enhancement of $\text{Re}[G^{\uparrow\downarrow}]$, leading to a large DL torque efficiency (up to 0.51) generated by the spin Hall effect in $\text{Bi}_{0.1}\text{Sb}_{0.9}$. These experimental and theoretical results demonstrate that engineering of inherent energy barriers in metallic spintronic devices provide a route to tailor the SOTs

torques.

We choose the topological semimetal $\text{Bi}_{0.1}\text{Sb}_{0.9}$ as the source of a diffusive spin current for two reasons. First, the formation of a metal/semimetal contact amplifies the effects of an interfacial energy barrier on spin transport compared to conventional metallic spin-orbitronic devices. The reason for this is that the carrier density of $\text{Bi}_x\text{Sb}_{1-x}$ alloys is at least an order of magnitude smaller than that of frequently used heavy metals, such as Pt, but much larger than that of semiconductors; the formation of a metal/semimetal contact results in an atomically thin carrier depletion layer on the semimetal side, as shown in Fig. 1b, which is prominent compared to that in metal/metal heterojunctions. Second, because of the presence of “hot spots” for Berry curvature in the Brillouin zone, the intrinsic spin Hall conductivity of $\text{Bi}_x\text{Sb}_{1-x}$ has been predicted to be comparable to that of heavy metals and much larger than that of semiconductors [23]. Along with a well-defined surface in Sb-rich films, these features make semimetallic $\text{Bi}_{0.1}\text{Sb}_{0.9}$ a promising source of a bulk spin current (see also Supplementary Note 1).

Results

SOTs generated by spin Hall effect

We first investigate the spin transport across a $\text{Ni}_{81}\text{Fe}_{19}/\text{Bi}_{0.1}\text{Sb}_{0.9}$ interface through SOT characterization combined with drift-diffusion analysis. $\text{Ni}_{81}\text{Fe}_{19}(6\text{ nm})/\text{Bi}_{0.1}\text{Sb}_{0.9}(t)$ bilayers are fabricated by radio frequency (RF) magnetron sputtering, where the numbers in parentheses represent the thickness t (see Methods for details). In Fig. 2a, we show cross-sectional transmission electron microscopy (TEM) images of the $\text{Ni}_{81}\text{Fe}_{19}/\text{Bi}_{0.1}\text{Sb}_{0.9}$ bilayer. The TEM images show grains with different crystallographic orientations in the $\text{Bi}_{0.1}\text{Sb}_{0.9}$ layer and a distinct interface between the $\text{Ni}_{81}\text{Fe}_{19}$ and $\text{Bi}_{0.1}\text{Sb}_{0.9}$ layers. The polycrystalline feature of the $\text{Bi}_{0.1}\text{Sb}_{0.9}$ layer with two preferred crystallographic orientations is consistent with the X-ray diffraction results, eliminating any possible variation in the microstructure upon changing the thickness (see Supplementary Note 1).

For the in-plane magnetized $\text{Ni}_{81}\text{Fe}_{19}/\text{Bi}_{0.1}\text{Sb}_{0.9}$ films, we measure the spin torque ferromagnetic resonance (ST-FMR) at room temperature, as shown in Fig. 2b. In the device, an in-plane RF current induces a transverse spin current in the $\text{Bi}_{0.1}\text{Sb}_{0.9}$ layer, diffusing towards the $\text{Ni}_{81}\text{Fe}_{19}$ layer. The spin transport across the $\text{Ni}_{81}\text{Fe}_{19}/\text{Bi}_{0.1}\text{Sb}_{0.9}$ interface gives rise to oscillating torques with a frequency f , including DL and FL torques,

exerted on the magnetization of the $\text{Ni}_{81}\text{Fe}_{19}$ layer under the FMR condition. In Fig. 2c, we show representative ST-FMR spectra at different f for the $\text{Ni}_{81}\text{Fe}_{19}/\text{Bi}_{0.1}\text{Sb}_{0.9}$ film with $t = 10$ nm. The ST-FMR spectra can be decomposed into symmetric ($L_{\text{sym}}(H) = W^2/[(\mu_0 H - \mu_0 H_{\text{FMR}})^2 + W^2]$) and antisymmetric ($L_{\text{asym}}(H) = W(\mu_0 H - \mu_0 H_{\text{FMR}})/[(\mu_0 H - \mu_0 H_{\text{FMR}})^2 + W^2]$) functions [24, 25]: $V_{\text{mix}} = V_{\text{s}}L_{\text{sym}}(H) + V_{\text{a}}L_{\text{asym}}(H)$, where W is the spectral width, H is the external magnetic field, and H_{FMR} is the FMR field. As shown in Fig. 2d, we observe a clear symmetric component V_{s} , determined by the DL effective field H_{DL} , as well as an antisymmetric component V_{a} , attributed to the sum of the FL effective field H_{FL} and the current-induced Oersted field H_{Oe} . We determine H_{DL} and H_{FL} by fitting the ST-FMR spectra at $f = 7$ GHz [26, 27], where the RF current I_{RF} flowing in the device is determined with a vector network analyzer (see Supplementary Note 2). The obtained H_{DL} and H_{FL} with different $\text{Bi}_{0.1}\text{Sb}_{0.9}$ thicknesses are further converted to the SOT efficiency per unit electric field E , $\xi_{\text{DL(FL)}}^E = (2e/\hbar)\mu_0 M_{\text{s}} t_{\text{F}} H_{\text{DL(FL)}}/E$, as shown in Fig. 3a, where e is the electron charge, \hbar is the reduced Planck constant, μ_0 is the vacuum permeability, M_{s} is the saturation magnetization, and t_{F} is the thickness of the magnetic layer.

Figure 3a shows that both ξ_{DL}^E and ξ_{FL}^E monotonically increase over a fairly long length scale with increasing the $\text{Bi}_{0.1}\text{Sb}_{0.9}$ layer thickness t . We also note that the magnitude of the FL torque efficiency ξ_{FL}^E dominates the DL torque efficiency ξ_{DL}^E at all t , which is in sharp contrast to the SOTs in conventional ferromagnetic-metal/heavy-metal devices, where ξ_{FL}^E is negligible compared to ξ_{DL}^E [28]. The thickness-dependent SOT efficiencies suggest that the SOTs originate from the bulk spin Hall effect in the $\text{Bi}_{0.1}\text{Sb}_{0.9}$ layer. However, unavoidable self-doping effects and the coexistence of topological surface states (TSSs) and bulk states in the topological semimetal may lead to anomalous thickness-dependent transport properties [29], which can subsequently be responsible for the unexpected behavior of thickness-dependent SOT generation. To test this possibility, we investigate the transport properties of the $\text{Bi}_{0.1}\text{Sb}_{0.9}$ layers with different t . As shown in Fig. 3b, the sheet resistance R_{sh} of the $\text{Bi}_{0.1}\text{Sb}_{0.9}$ film is nearly proportional to $1/t$ at room temperature. This result indicates that the transport is dominated by the bulk conduction. In fact, the three-dimensional (3D) resistivity ρ is well reproduced by an empirical model that takes into account the carrier reflection at the surface, as shown in Fig. 3c, demonstrating the bulk-dominated conduction with invariable transport properties upon changing the thickness (see Supplementary Note 3). We also note that the temperature dependence

of the conductivity, with an analysis based on a parallel conduction model, suggests the presence of a small hopping term incorporated into the total conduction [30, 31]. The nearly thickness-independent contribution of the metallic channel to the total conductivity ~ 0.93 reflects the disordered nature but stable transport properties of the sputtered $\text{Bi}_{0.1}\text{Sb}_{0.9}$ films (see Supplementary Note 4).

On the basis of the bulk-dominated conduction with the invariable transport properties, we attribute the thickness-dependent SOT efficiencies to an intrinsic bulk feature of the disordered topological semimetal $\text{Bi}_{0.1}\text{Sb}_{0.9}$. The SOTs induced by the spin Hall effect are described by employing a drift-diffusion approach, where the spin transport at the interface is governed by the complex spin mixing conductance $G^{\uparrow\downarrow}$ [6, 32]:

$$\xi_{\text{DL}}^E = \frac{2e}{\hbar} \sigma_s [1 - \text{sech}(t/\lambda_s)] \frac{2\lambda_s \rho_{\text{BiSb}} \text{Re}[G^{\uparrow\downarrow}] [2\lambda_s \rho_{\text{BiSb}} \text{Re}[G^{\uparrow\downarrow}] + \tanh(t/\lambda_s)] + (2\lambda_s \rho_{\text{BiSb}} \text{Im}[G^{\uparrow\downarrow}])^2}{[2\lambda_s \rho_{\text{BiSb}} \text{Re}[G^{\uparrow\downarrow}] + \tanh(t/\lambda_s)]^2 + (2\lambda_s \rho_{\text{BiSb}} \text{Im}[G^{\uparrow\downarrow}])^2}, \quad (1)$$

$$\xi_{\text{FL}}^E = -\frac{2e}{\hbar} \sigma_s [1 - \text{sech}(t/\lambda_s)] \frac{2\lambda_s \rho_{\text{BiSb}} \text{Im}[G^{\uparrow\downarrow}] \tanh(t/\lambda_s)}{[2\lambda_s \rho_{\text{BiSb}} \text{Re}[G^{\uparrow\downarrow}] + \tanh(t/\lambda_s)]^2 + (2\lambda_s \rho_{\text{BiSb}} \text{Im}[G^{\uparrow\downarrow}])^2}. \quad (2)$$

With the extracted $\text{Bi}_{0.1}\text{Sb}_{0.9}$ bulk resistivity, $\rho_{\text{BiSb}} = 350.3 \mu\Omega\text{cm}$, equations (1) and (2) fit the t dependence of ξ_{DL}^E and ξ_{FL}^E fairly well, as shown in Fig. 3a, providing the real and imaginary parts of the spin mixing conductance as $\text{Re}[G^{\uparrow\downarrow}] = 0.023 \times 10^{13} \Omega^{-1}\text{m}^{-2}$ and $\text{Im}[G^{\uparrow\downarrow}] = 0.133 \times 10^{13} \Omega^{-1}\text{m}^{-2}$, respectively. From the fitting, we also obtain the spin diffusion length $\lambda_s = 24.8 \pm 1.0 \text{ nm}$, which is much longer than that of normal metal SOT source materials, including Pt (2.0 nm) [33], β -Ta (2.5 nm) [34] and W (1.5 nm) [35], determined by a similar analysis based on SOT characterization. The bulk spin Hall conductivity in $\text{Bi}_{0.1}\text{Sb}_{0.9}$ is extracted as $\sigma_s = (3.68 \pm 0.17) \times 10^5 (\hbar/2e) \Omega^{-1} \text{m}^{-1}$ (see also Supplementary Note 5).

SOTs governed by inherent energy barrier

A striking feature of the SOT generation in the $\text{Ni}_{81}\text{Fe}_{19}/\text{Bi}_{0.1}\text{Sb}_{0.9}$ bilayers is that the FL torque and $\text{Im}[G^{\uparrow\downarrow}]$ are much larger than the DL torque and $\text{Re}[G^{\uparrow\downarrow}]$, respectively, in sharp contrast to the conventional bulk-dominated SOTs and the spin mixing conductance in metallic devices. It is known that spin transport across a non-magnetic/magnetic interface is well characterized by the spin mixing conductance based on magnetoelectronic circuit theory [16]. In this model, the real part of the spin mixing conductance, $\text{Re}[G^{\uparrow\downarrow}]$, determines the spin transmission associated with the DL-torque generation and the imaginary part of

the spin mixing conductance, $\text{Im}[G^{\uparrow\downarrow}]$, determines the reflection of spins exchange coupled to the interfacial magnetization associated with the FL-torque generation (see equations (1) and (2)). We note that the extracted $\text{Re}[G^{\uparrow\downarrow}]$ is more than three orders of magnitude smaller than that of the $\text{Ni}_{81}\text{Fe}_{19}/\text{Pt}$ interface [36]. At intermetallic interfaces, $\text{Re}[G^{\uparrow\downarrow}]$ is close to the Sharvin conductance $G_{\text{Sh}} = (1/\hbar)(ek_{\text{F}}/2\pi)^2$, which is the limit of the spin mixing conductance, where k_{F} is the Fermi wavenumber [37, 38]. In such system, $\text{Re}[G^{\uparrow\downarrow}]$ is much larger than $\text{Im}[G^{\uparrow\downarrow}]$. For a simple 3D isotropic Fermi surface, $\text{Re}[G^{\uparrow\downarrow}]$ is proportional to $n^{2/3}$ because $k_{\text{F}} = (3\pi^2 n)^{1/3}$, where n is the carrier density, suggesting that $\text{Re}[G^{\uparrow\downarrow}]$ is smaller for materials with lower carrier density. However, the large difference in $\text{Re}[G^{\uparrow\downarrow}]$ between the $\text{Ni}_{81}\text{Fe}_{19}/\text{Bi}_{0.1}\text{Sb}_{0.9}$ and $\text{Ni}_{81}\text{Fe}_{19}/\text{Pt}$ interfaces cannot be attributed to the difference in the carrier density between $\text{Bi}_{0.1}\text{Sb}_{0.9}$ and Pt; the carrier density of the disordered $\text{Bi}_{0.1}\text{Sb}_{0.9}$ film is in the range of $0.1 \times 10^{21} \text{ cm}^{-3} < n < 1.2 \times 10^{21} \text{ cm}^{-3}$ (Supplementary Note 6), while that of Pt is $1.6 \times 10^{22} \text{ cm}^{-3}$ [39], giving a $\text{Re}[G^{\uparrow\downarrow}] (\text{Pt})/\text{Re}[G^{\uparrow\downarrow}] (\text{Bi}_{0.1}\text{Sb}_{0.9})$ ratio of less than 30. Here, the small $\text{Re}[G^{\uparrow\downarrow}]$ in the $\text{Ni}_{81}\text{Fe}_{19}/\text{Bi}_{0.1}\text{Sb}_{0.9}$ bilayer is also confirmed by measuring the magnetic damping (see also Supplementary Note 7).

The unconventional feature of the SOTs and spin mixing conductance in the $\text{Ni}_{81}\text{Fe}_{19}/\text{Bi}_{0.1}\text{Sb}_{0.9}$ heterostructure can be attributed to the formation of an energy barrier at the interface. At the interface of metallic heterostructures, a mismatch of the work functions ϕ of the two metals leads to the formation of an interfacial energy barrier, arising from the creation of a carrier depletion region. In the $\text{Ni}_{81}\text{Fe}_{19}/\text{Bi}_{0.1}\text{Sb}_{0.9}$ junction, the work function of $\text{Ni}_{81}\text{Fe}_{19}$ is $\phi_{\text{Ni}_{81}\text{Fe}_{19}} = 4.83 \text{ eV}$ [40], while that of $\phi_{\text{Bi}_{0.1}\text{Sb}_{0.9}}$ is estimated to be $\phi_{\text{Bi}_{0.1}\text{Sb}_{0.9}} \sim 4.55 \text{ eV}$ by adopting a two-component alloy model with the work functions of Bi and Sb (Supplementary Note 8). As a result, electron transfer from the $\text{Bi}_{0.1}\text{Sb}_{0.9}$ layer to the $\text{Ni}_{81}\text{Fe}_{19}$ layer appears upon equilibration of the Fermi levels, resulting in the formation of a depletion region of electrons at the atomic scale in the vicinity of the $\text{Bi}_{0.1}\text{Sb}_{0.9}$ side of the $\text{Ni}_{81}\text{Fe}_{19}/\text{Bi}_{0.1}\text{Sb}_{0.9}$ interface. Since the resulting barrier at the $\text{Ni}_{81}\text{Fe}_{19}/\text{Bi}_{0.1}\text{Sb}_{0.9}$ interface is much thinner than that at metal/semiconductor interfaces, no signature of the barrier can be found from current-voltage measurements across the interface. Nevertheless, we observed the unconventional feature of the spin mixing conductance; $\text{Im}[G^{\uparrow\downarrow}]$ is much larger than $\text{Re}[G^{\uparrow\downarrow}]$ in the metallic bilayer, which suggests sizable spin-dependent reflection at the interface. This result is in sharp contrast to the conventional wisdom that $\text{Im}[G^{\uparrow\downarrow}]$ is very small in metallic interfaces [41–45]. This observation demonstrates that even the

ultrathin inherent barrier governs the spin mixing conductance and the corresponding SOT generation, which has been overlooked so far. Note that this energy barrier occurs for the transport of both electrons in the conduction band and holes in the valence band from the $\text{Bi}_{0.1}\text{Sb}_{0.9}$ layer to the $\text{Ni}_{81}\text{Fe}_{19}$ layer. Regarding the energy band diagram, a distinct feature of semimetals is that the Fermi level is located above the conduction band minimum and below the valence band maximum (Fig. 1b), rather than pinned in the band gap as in semiconductors (Fig. 1a). Since the Fermi level of $\text{Bi}_{0.1}\text{Sb}_{0.9}$ lies less than ~ 0.16 eV above the conduction band maximum at the L point in the Brillouin zone [46], the interfacial charge transfer gives rise to an electron energy barrier for the spin transport from the $\text{Bi}_{0.1}\text{Sb}_{0.9}$ layer to the $\text{Ni}_{81}\text{Fe}_{19}$ layer. Since the conduction of the $\text{Bi}_{0.1}\text{Sb}_{0.9}$ layer is dominated by hole transport (Supplementary Note 6), taking the hole spin transport across the interface into account is essential. In describing the hole injection from the $\text{Bi}_{0.1}\text{Sb}_{0.9}$ layer to the $\text{Ni}_{81}\text{Fe}_{19}$ layer, or its equivalent electron transport from the $\text{Ni}_{81}\text{Fe}_{19}$ layer to the valence band of the $\text{Bi}_{0.1}\text{Sb}_{0.9}$ layer, one can expect an even higher energy barrier owing to the band bending of the valence band above the Fermi level, as illustrated in Fig. 3d. This corresponds to an energy barrier for the hole spin transport.

To uncover the microscopic origin of the large imaginary part of the spin mixing conductance in the $\text{Ni}_{81}\text{Fe}_{19}/\text{Bi}_{0.1}\text{Sb}_{0.9}$ bilayer, we model the depletion region and emergent energy barrier between magnetic-metal and semimetal layers by an interfacial potential barrier consisting of a spin-independent part and a spin-dependent part. Within the microscopic tight-binding formalism, we model the electron hopping through this interfacial potential barrier by a spin-independent hopping amplitude δt and a spin-dependent hopping amplitude J (see Fig. 4a). Using a 3D scattering formalism [47–49], we compute the real and imaginary parts of the spin mixing conductance (Supplementary Note 9). Figures 4b and 4c summarize our analytical results. In Fig. 4b, we show that depending on the spin-dependent hopping amplitude J , the imaginary part of the spin mixing conductance may be an order of magnitude larger than its real part. Notably, another significant feature is that the interfacial hopping modifies the real part of the spin mixing conductance, which may lead to orders of magnitude enhancement with decreasing size of the energy barrier, as shown in Fig. 4c.

Energy barrier engineering of SOTs

To verify the generality of the concept of an energy barrier effect on spin transport across metallic heterostructures, we perform a cross check by quantifying the SOT efficiency for perpendicularly magnetized $\text{Co}_{72}\text{Tb}_{28}(6\text{ nm})/\text{Bi}_{0.1}\text{Sb}_{0.9}(t)$ films with another widely used harmonic technique. The choice of the Tb-based metallic magnet is due to the low work function of Tb (3 eV), which can minimize the effect of an energy barrier compared to the $\text{Ni}_{81}\text{Fe}_{19}/\text{Bi}_{0.1}\text{Sb}_{0.9}$ films. The work function of $\text{Co}_{72}\text{Tb}_{28}$ is $\phi_{\text{Co}_{72}\text{Tb}_{28}} \sim 4.47\text{ eV}$ ($< \phi_{\text{Bi}_{0.1}\text{Sb}_{0.9}} \sim 4.55\text{ eV}$), and hence there is nearly no energy barrier formed on the $\text{Bi}_{0.1}\text{Sb}_{0.9}$ side, as illustrated in Fig. 3e. We employ the out-of-plane angular-dependent harmonic Hall measurement technique to characterize the direction and magnitude of the DL torque for the perpendicularly magnetized device at room temperature (see Fig. 5a) [50].

In Fig. 5b, we show the first and second harmonic Hall resistances, R_ω and $R_{2\omega}$, measured by rotating the external magnetic field in the xz plane. In this result, the contributions from the ordinary Hall effect and the ordinary Nernst effect have been subtracted from the measured first and second harmonic signals, respectively (Supplementary Note 10). We estimate the out-of-plane angle θ_M of the net magnetization at each magnetic field angle θ_H using $\theta_M = \arccos(R_\omega/R_{\text{AHE}}) - \pi$, where R_{AHE} is the anomalous Hall coefficient. Here, the $-\pi$ term arises from the fact that the transport measurement detects the direction of the magnetization of Co because the $4f$ band of Tb is well below the Fermi level, while the net magnetization is dominated by Tb in the $\text{Co}_{72}\text{Tb}_{28}$ film. As shown in Fig. 5b, the change in R_ω as a function of θ_M opens upwards, which is consistent with the picture of Tb-dominated net magnetization. Using $dR_{2\omega}/d(\sin \theta_M) = -R_{2\omega}^{\text{ANE}} - (1/2)R_{\text{AHE}}H_{\text{DL}}[1 - 4(R_{\text{PHE}}/R_{\text{AHE}})^2]/(H + H_K)$, we determine the DL torque efficiency ξ_{DL}^E for the $\text{Co}_{72}\text{Tb}_{28}/\text{Bi}_{0.1}\text{Sb}_{0.9}$ film, where $R_{2\omega}^{\text{ANE}}$ is the second harmonic signal due to the anomalous Nernst effect, H_K is the anisotropy field, and R_{PHE} is the planar Hall resistance (Supplementary Notes 10 and 11). In Fig. 3a, we plot the DL torque efficiency for the $\text{Co}_{72}\text{Tb}_{28}/\text{Bi}_{0.1}\text{Sb}_{0.9}$ film. This result provides further evidence of the thickness-dependent ξ_{DL}^E . The sign of ξ_{DL}^E in the $\text{Co}_{72}\text{Tb}_{28}/\text{Bi}_{0.1}\text{Sb}_{0.9}$ film is the same as that in the $\text{Ni}_{81}\text{Fe}_{19}/\text{Bi}_{0.1}\text{Sb}_{0.9}$ film but opposite to that generated by a Co-Tb single-layer film [51], supporting that the DL torque originates from the bulk spin Hall effect in the $\text{Bi}_{0.1}\text{Sb}_{0.9}$ layer.

We find that the topological semimetal $\text{Bi}_{0.1}\text{Sb}_{0.9}$ becomes an efficient source of the SOT through energy barrier engineering, i.e., minimizing the mismatch of the work

functions of the magnetic layer and the $\text{Bi}_{0.1}\text{Sb}_{0.9}$ layer. Figure 3a shows that the ξ_{DL}^E of the $\text{Co}_{72}\text{Tb}_{28}/\text{Bi}_{0.1}\text{Sb}_{0.9}$ bilayer is more than eight times greater than that of the $\text{Ni}_{81}\text{Fe}_{19}/\text{Bi}_{0.1}\text{Sb}_{0.9}$ bilayer when $t = 26$ nm. These sizable DL torques are further confirmed by performing magnetization switching on $\text{Co}_{72}\text{Tb}_{28}/\text{Bi}_{0.1}\text{Sb}_{0.9}$ with strong perpendicular magnetic anisotropy (see Supplementary Note 12). Note that a DL-torque enhancement due to an exchange torque near the magnetization compensation point, such as that observed in $\text{Co}_{1-x}\text{Gd}_x/\text{Pt}$ [52], is unlikely to occur in the $\text{Co}_{72}\text{Tb}_{28}/\text{Bi}_{0.1}\text{Sb}_{0.9}$ films since the spin Hall angle is nearly unchanged in $\text{Co}_{1-x}\text{Tb}_x/\text{Ta}$ upon changing the Tb concentration [53]. We also note that the clear difference in ξ_{DL}^E between the $\text{Ni}_{81}\text{Fe}_{19}/\text{Bi}_{0.1}\text{Sb}_{0.9}$ and the $\text{Co}_{72}\text{Tb}_{28}/\text{Bi}_{0.1}\text{Sb}_{0.9}$ films cannot primarily be attributed to a potential discrepancy in the estimated efficiencies produced by the different characterization techniques [27].

The enhancement of the DL torque efficiency is more likely associated with an enhancement in $\text{Re}[G^{\uparrow\downarrow}]$. We obtain $\text{Re}[G^{\uparrow\downarrow}] = 7.11 \times 10^{13} \Omega^{-1}\text{m}^{-2}$ at the $\text{Co}_{72}\text{Tb}_{28}/\text{Bi}_{0.1}\text{Sb}_{0.9}$ interface by fitting the t dependence of ξ_{DL}^E for the $\text{Co}_{72}\text{Tb}_{28}/\text{Bi}_{0.1}\text{Sb}_{0.9}$ bilayer using equation (1) with the σ_s and $\lambda_s \rho_{\text{BiSb}}$ values obtained from the results for the $\text{Ni}_{81}\text{Fe}_{19}/\text{Bi}_{0.1}\text{Sb}_{0.9}$ device and under the assumption of $\text{Im}[G^{\uparrow\downarrow}] \ll \text{Re}[G^{\uparrow\downarrow}]$ due to the vanished energy barrier (see also Supplementary Note 13), where the dimensionless parameter of the spin-dependent hopping is expected to be in the range of 0.5 to 1. This result suggests that $\text{Re}[G^{\uparrow\downarrow}]$ is enhanced by more than two orders of magnitude by replacing $\text{Ni}_{81}\text{Fe}_{19}$ with $\text{Co}_{72}\text{Tb}_{28}$. The estimated value of $\text{Re}[G^{\uparrow\downarrow}]$ at the $\text{Co}_{72}\text{Tb}_{28}/\text{Bi}_{0.1}\text{Sb}_{0.9}$ interface is close to the Sharvin conductance of $\text{Bi}_{0.1}\text{Sb}_{0.9}$, which is in the range of $3 \times 10^{13} \Omega^{-1}\text{m}^{-2}$ to $17 \times 10^{13} \Omega^{-1}\text{m}^{-2}$. Here, the maximum ξ_{DL}^E in the $\text{Co}_{72}\text{Tb}_{28}/\text{Bi}_{0.1}\text{Sb}_{0.9}$ film corresponds to the dimensionless DL torque efficiency, or the effective spin Hall angle, of $\xi_{\text{DL}} = \xi_{\text{DL}}^E \rho = 0.51 \pm 0.18$ (see also Supplementary Note 1). This value is larger than that in SOT devices with widely used heavy metals, such as Pt and Ta, and is comparable to that in a SOT device with a recently proposed heavy metal alloy, $\text{Au}_{0.25}\text{Pt}_{0.75}$, with $\xi_{\text{DL}} = 0.35$ [54] (see Supplementary Table I).

To further capture the characteristics of the SOTs originating from the spin Hall effect in topological semimetals, we measure temperature T dependence of the DL torque efficiency ξ_{DL}^E for the $\text{Co}_{72}\text{Tb}_{28}(6 \text{ nm})/\text{Bi}_{0.1}\text{Sb}_{0.9}(10 \text{ nm})$ film, where the interfacial barrier can be neglected. As shown in Fig. 5c, ξ_{DL}^E is almost independent of T in the $\text{Co}_{72}\text{Tb}_{28}/\text{Bi}_{0.1}\text{Sb}_{0.9}$ bilayer. This result is different from the T dependence of the DL torque efficiency in

heterostructures consisted of Bi/Sb multilayers ($\text{Bi}_x\text{Sb}_{1-x}$) and CoFeB, where the DL torque efficiency has been found to be suppressed at low T [55]. We note that the spin transport in the $\text{Bi}_x\text{Sb}_{1-x}/\text{CoFeB}$ film can be affected by an interfacial barrier. In the $\text{Bi}_x\text{Sb}_{1-x}/\text{CoFeB}$ films, the CoFeB layer is interfaced with Bi. Since the work function of Bi, 4.34 eV, is smaller than that of CoFeB, 4.83 eV, an energy barrier is formed at the $\text{Bi}_x\text{Sb}_{1-x}/\text{CoFeB}$ interface. The observed T -dependent behavior in the $\text{Bi}_x\text{Sb}_{1-x}/\text{CoFeB}$ films can be understood in terms of spin transport modulated by the thermionic emission; in the presence of the energy barrier, the thermal activation of electrons plays an important role in the electron transport across the interface, which subsequently modifies the spin transport and torque generation efficiency. The suppression of the torque efficiency at low T in the $\text{Bi}_x\text{Sb}_{1-x}/\text{CoFeB}$ structure might be highly related to the suppression of the spin transmission due to the thermionic emission. In contrast to the $\text{Bi}_x\text{Sb}_{1-x}/\text{CoFeB}$ structure, no energy barrier is expected to be present at the $\text{Co}_{72}\text{Tb}_{28}/\text{Bi}_{0.1}\text{Sb}_{0.9}$ interface, and thus this mechanism is absent in the $\text{Co}_{72}\text{Tb}_{28}/\text{Bi}_{0.1}\text{Sb}_{0.9}$ bilayer.

The nearly T -independent ξ_{DL}^E observed for the $\text{Co}_{72}\text{Tb}_{28}/\text{Bi}_{0.1}\text{Sb}_{0.9}$ bilayer is consistent with the torque generation originating from the bulk spin Hall effect and spin transmission free from an energy barrier. Considering the fact that the bulk resistivity of the $\text{Bi}_{0.1}\text{Sb}_{0.9}$ layer ($350.3 \mu\Omega\text{m}$) falls in the dirty metallic regime, the spin Hall conductivity or ξ_{DL}^E should scale with the electrical conductivity of the $\text{Bi}_{0.1}\text{Sb}_{0.9}$ layer. However, we found that a change in the conductivity of the $\text{Bi}_{0.1}\text{Sb}_{0.9}$ layer is only less than 9% upon lowering T from 300 K to 20 K (see Supplementary Note 4). This result indicates that the spin Hall conductivity barely changes with T , which is consistent with the nearly T -independent ξ_{DL}^E , shown in Fig. 5c. While nontrivial surface states may also be present in the $\text{Bi}_{0.1}\text{Sb}_{0.9}$ layer (see Supplementary Note 14), the T -independent behaviour eliminates the possible contribution from the surface states to the DL torque because this contribution is expected to be enhanced at low T [56, 57]. The minor role of the surface states in generating the DL torque is consistent with the strong $\text{Bi}_{0.1}\text{Sb}_{0.9}$ -thickness dependence of the DL torque efficiency, shown in Fig. 3, which evidences the bulk-dominated DL torque generation.

Summary and outlook

In this work, we have presented the concept of the SOTs governed by an inherent energy barrier in metallic contacts. Experimentally, by measuring the ST-FMR, we found that the

DL and FL torque efficiencies in the $\text{Ni}_{81}\text{Fe}_{19}/\text{Bi}_{0.1}\text{Sb}_{0.9}$ bilayer increase with the $\text{Bi}_{0.1}\text{Sb}_{0.9}$ thickness, indicating that both SOTs originate from the bulk spin Hall effect. This finding allows us to analyze the $\text{Bi}_{0.1}\text{Sb}_{0.9}$ -thickness dependence of the DL and FL torque efficiencies based on the drift-diffusion approach where the interfacial spin transfer is characterized by the spin mixing conductance. This analysis enables us to extract the real and imaginary parts of the spin mixing conductance as $\text{Re}[G^{\uparrow\downarrow}] = 0.023 \times 10^{13} \Omega^{-1}\text{m}^{-2}$ and $\text{Im}[G^{\uparrow\downarrow}] = 0.133 \times 10^{13} \Omega^{-1}\text{m}^{-2}$, respectively. The extracted real part of the spin mixing conductance is two-orders of magnitude smaller than the Sharvin conductance of $\text{Bi}_{0.1}\text{Sb}_{0.9}$. This finding supports the existence of an interfacial energy barrier, which is consistent with the analysis of the work function mismatch. The crucial role of the interfacial barrier in generating the SOTs is further supported by our calculation. As a cross-check, we also aimed to quantify the SOT efficiencies in a $\text{Bi}_{0.1}\text{Sb}_{0.9}$ -based system without an interfacial energy barrier. From our analysis of work function mismatch, we found that the $\text{Co}_{72}\text{Tb}_{28}/\text{Bi}_{0.1}\text{Sb}_{0.9}$ bilayer meets this requirement. However, the large magnetic damping in $\text{Co}_{72}\text{Tb}_{28}$ makes it difficult to quantify the SOT efficiencies for the $\text{Co}_{72}\text{Tb}_{28}/\text{Bi}_{0.1}\text{Sb}_{0.9}$ bilayer by the ST-FMR. Therefore, instead of ST-FMR, we used the second harmonic technique, which is widely considered to be the most reliable for characterizing the SOT efficiency of perpendicularly magnetized films. By taking into account all possible contributions, such as Nernst signals, we extracted the DL-SOT efficiency for the $\text{Co}_{72}\text{Tb}_{28}/\text{Bi}_{0.1}\text{Sb}_{0.9}$ bilayer. The result shows that the DL-SOT efficiency of the $\text{Co}_{72}\text{Tb}_{28}/\text{Bi}_{0.1}\text{Sb}_{0.9}$ bilayer is clearly higher than that of the $\text{Ni}_{81}\text{Fe}_{19}/\text{Bi}_{0.1}\text{Sb}_{0.9}$ bilayer. The corresponding real part of the spin mixing conductance, $\text{Re}[G^{\uparrow\downarrow}] = 7.11 \times 10^{13} \Omega^{-1}\text{m}^{-2}$, of the $\text{Co}_{72}\text{Tb}_{28}/\text{Bi}_{0.1}\text{Sb}_{0.9}$ bilayer is found to be close to the Sharvin conductance, as expected from the minor role of the interfacial barrier due to the lower work function of $\text{Co}_{72}\text{Tb}_{28}$.

The above experimental and theoretical observations support the scenario that an inherent barrier governs the SOT generation even in metallic contacts. However, the use of the two different experimental techniques for the SOT characterization could potentially lead to a large discrepancy between the estimated torque efficiencies if artifact contributions dominate the detected signals. To avoid this risk, we have carefully designed our experiments to clarify the role of an interfacial energy barrier in the generation of the SOTs. This includes the comparison of the FL and DL torque efficiencies, the evaluation of the spin mixing conductance, the analysis of work function mismatch, and the development of the theoretical model. We have carefully checked the validity of the ST-FMR analysis (see Supplementary

Note 2). We also note that the tiny $\text{Re}[G^{\uparrow\downarrow}]$ suggested by the SOTs in the $\text{Ni}_{81}\text{Fe}_{19}/\text{Bi}_{0.1}\text{Sb}_{0.9}$ bilayer is supported by the magnetic damping measurement (see Supplementary Note 7). We believe that these results provide evidence for the essential role of the inherent barrier in the generation of the SOTs. Here, in this work, we focus on the $\text{Co}_{72}\text{Tb}_{28}/\text{Bi}_{0.1}\text{Sb}_{0.9}$ bilayer for the temperature-dependent measurement. At the $\text{Ni}_{81}\text{Fe}_{19}/\text{Bi}_{0.1}\text{Sb}_{0.9}$ interface, the presence of finite roughness and stacking faults can introduce atomic inhomogeneity, potentially leading to variations in the energy barrier. Consequently, the temperature-dependent behavior of spin transport across the interfacial energy barrier may be more complex than a simple model of thermionic emission [58]. Further systematic studies are required to fully understand the SOT generation in the presence of inherent barriers, which presents an interesting topic for future research.

The SOTs observed in $\text{Ni}_{81}\text{Fe}_{19}/\text{Bi}_{0.1}\text{Sb}_{0.9}$ bilayer are characterized by the large $\text{Im}[G^{\uparrow\downarrow}]/\text{Re}[G^{\uparrow\downarrow}]$ ratio even though their origin is the bulk spin Hall effect. This character is different from the widely studied SOTs associated with interfacial spin-orbit coupling in metallic systems [59]. In the latter scenario, the interfacial spin-flip scattering modulates the spin transmission probability across the interface, where the discontinuity of the spin current depends on the strength of the interfacial spin-orbit coupling. This effect, known as spin memory loss, is manifested as a vanishingly small $\text{Im}[G^{\uparrow\downarrow}]$ compared to $\text{Re}[G^{\uparrow\downarrow}]$. Different from this scenario, our experimental and theoretical results show that an energy barrier due to the formation of a carrier depletion region governs the spin mixing conductance by modifying the amplitudes of the spin-dependent and spin-independent hopping. This subsequently has a significant impact on the generation of FL and DL torques.

The role of interfacial barriers in electrical spin injection in ferromagnetic-metal/semiconductor junctions has been discussed over the past two decades. The role of interfacial barriers in the SOT generation by the spin Hall effect is clearly different from that in the electrical spin injection into semiconductors. In the electrical spin injection into a semiconductor, an electric voltage is applied across a ferromagnetic-metal/semiconductor interface. An interfacial barrier, including a Schottky barrier and an artificial insertion layer, has been used to improve the spin transmission efficiency across the interface because it allows to circumvent the impedance mismatch problem [4]. In contrast, in the SOT generation by the spin Hall effect, spin-dependent reflection is promoted by an inherent barrier, resulting in the sizable FL torque in the metallic bilayers. It is important to note that due to the extremely

low spin transmission probability across Schottky or oxide-insertion layers in the diffusive regime, it has been challenging to investigate the generation of SOTs through a combination of experimental and theoretical studies. Our results demonstrate that an ultrathin energy barrier, naturally formed at the magnetic-metal/semimetal interface, significantly impacts the spin mixing conductance. This provides a unique opportunity to uncover the physics of the generation of SOTs in metallic heterostructures.

Our experimental and theoretical results demonstrate that energy barriers inherent in metallic spintronic devices are the key to control the FL and DL torques. The high carrier density of heavy metals limits the efficient control of the spin Hall effect and SOTs. The advantages of semimetals, such as $\text{Bi}_{0.1}\text{Sb}_{0.9}$, in terms of their relatively low carrier density with sizable SOT generation efficiencies allow to create ultrathin energy barriers, providing a possible route to simultaneously tailor the FL and the DL torques. Of particular importance is that the results open a route to tailor the FL torque by interface engineering. Recent advances in spin-orbitronics have demonstrated the crucial role of the FL torque in spin-orbitronic phenomena and functionalities. In particular, the FL torque dynamically influences the magnetic domain wall chirality, which is a key element for improving the SOT switching efficiency [60] and realizing unipolar magnetization switching [61]. More recently, a large FL torque is predicted to be crucial for ultrafast and highly efficient field-free switching [62].

The formation of an interfacial energy barrier in semimetal-based heterojunctions is a general effect when the Fermi level of the semimetal lies above that of the metal. Given the growing interest in utilizing novel materials such as topological semimetals, including Dirac and Weyl semimetals [63, 64], and metallic van der Waals ferromagnets [65, 66], our results highlight the crucial role of interfacial energy barriers in the pursuit of high-performance spintronic devices. Moreover, the impact of inherent barriers on the spin mixing conductance is not only important for the generation of SOTs but also for a variety of phenomena induced by spin transport, such as spin Hall magnetoresistance, spin Seebeck effect, and spin pumping. Therefore, our results shed light on the importance of inherent energy barriers, ubiquitous in heterojunctions, in the engineering of spintronic devices and understanding of spintronic phenomena.

Methods

Device fabrication. All films were grown on thermally oxidized Si substrates at room temperature by RF magnetron sputtering. A $\text{Bi}_{0.1}\text{Sb}_{0.9}$ layer with a thickness t ranging from 6 to 70 nm was first deposited using a composite $\text{Bi}_{0.1}\text{Sb}_{0.9}$ target with the base pressure of the chamber less than 1×10^{-5} Pa. The composition of the $\text{Bi}_{0.1}\text{Sb}_{0.9}$ films was confirmed by energy-dispersive X-ray spectroscopy. The Ar pressure during the deposition was fixed at 0.25 Pa, and an RF power of 70 W yielded a sputtering rate of 3.2 Å/s. For the transport measurements, the $\text{Bi}_{0.1}\text{Sb}_{0.9}$ single-layer films were patterned into Hall bars with a width of 250 μm and a length of 1050 μm using the shadow mask technique. The film surface was capped by 2.5-nm-thick Al_2O_3 to prevent oxidation. For the devices used for ST-FMR measurements, the $\text{Ni}_{81}\text{Fe}_{19}$ layer was grown on the $\text{Bi}_{0.1}\text{Sb}_{0.9}$ layer at a deposition rate of 0.5 Å/s, followed by a 2.5 nm-thick Al_2O_3 capping layer. The bilayer films were patterned into rectangular strips with a width of 7 μm and a length of 49 μm by photolithography and lift-off techniques. For the devices used for second harmonic measurements, the $\text{Co}_{72}\text{Tb}_{28}$ layer was prepared by cosputtering Co and Tb targets directly on top of the $\text{Bi}_{0.1}\text{Sb}_{0.9}$ layer and subsequently capped by 3-nm-thick Al to prevent oxidation. The RF power for the Co target was 120 W, and that for the Tb target was 49 W. The composition of the films was determined from the well-calibrated deposition rate. For the second harmonic measurements, the films were patterned into Hall cross bar devices with a width of 10 μm and a length of 40 μm using photolithography with a negative resist followed by Ar-ion milling and lift-off techniques.

Spin-torque ferromagnetic resonance. The SOTs of the in-plane magnetized $\text{Ni}_{81}\text{Fe}_{19}/\text{Bi}_{0.1}\text{Sb}_{0.9}$ bilayer films were characterized by ST-FMR. For the measurement, an RF current was applied to the device along its longitudinal direction using an analogue signal generator. The rectified voltage generated from the mixing of the RF current and the oscillating resistance due to the magnetization precession of the $\text{Ni}_{81}\text{Fe}_{19}$ layer was detected on the inductive side of the bias tee with a nanovoltmeter. To measure the RF current flowing in the device, the transmission and reflection coefficients were determined using a vector network analyser in the relevant frequency range (4-10 GHz).

Second harmonic measurements. For the perpendicular magnetized $\text{Co}_{72}\text{Tb}_{28}/\text{Bi}_{0.1}\text{Sb}_{0.9}$ bilayer films, we employed the out-of-plane angular-dependent harmonic Hall measurement

technique to characterize the SOTs. This method allows contributions from the anomalous Nernst effect and the ordinary Nernst effect to the second harmonic voltage to be eliminated. The latter can dominate the signal, leading to overestimation of the spin Hall conductivity in topological insulators and semimetals. During the measurement, an alternating current with a frequency of 85 Hz was injected into the device using a multifunction generator. The magnetic field slightly deviated from the film normal direction and was rotated in the out-of-plane direction of the sample, where the net magnetization coherently rotated with the external field and no magnetic multidomains were formed. The first and second harmonic Hall voltages were simultaneously detected using two lock-in amplifiers triggered at the same frequency by a current source.

Data availability

The data that support the findings of this study are available from the corresponding author upon reasonable request.

References

- [1] Schottky, W. Theory of blocking layer and point rectifiers. *Z. Phys* **113**, 367–414 (1939).
- [2] Mott, N. F. The theory of crystal rectifiers. *Proc. R. Soc. A* **171**, 27–38 (1939).
- [3] Razavieh, A., Zeitzoff, P. & Nowak, E. J. Challenges and limitations of CMOS scaling for FinFET and beyond architectures. *IEEE Trans. NanoTechnol.* **18**, 999–1004 (2019).
- [4] Žutić, I., Fabian, J. & Das Sarma, S. Spintronics: Fundamentals and applications. *Rev. Mod. Phys.* **76**, 323–410 (2004).
- [5] Hellman, F. *et al.* Interface-induced phenomena in magnetism. *Rev. Mod. Phys.* **89**, 025006 (2017).
- [6] Manchon, A. *et al.* Current-induced spin-orbit torques in ferromagnetic and antiferromagnetic systems. *Rev. Mod. Phys.* **91**, 035004 (2019).
- [7] Dyakonov, M. I. & Perel, V. I. Current-induced spin orientation of electrons in semiconductors. *Phys. Lett.* **35A**, 459–460 (1971).
- [8] Bychkov, Y. A. Properties of 2D electron gas with lifted spectral degeneracy. *JETP lett.* **39**, 78–81 (1984).
- [9] Edelstein, V. M. Spin polarization of conduction electrons induced by electric current in two-dimensional asymmetric electron systems. *Solid State Commun.* **73**, 233–235 (1990).
- [10] Qaiumzadeh, A., Duine, R. A. & Titov, M. Spin-orbit torques in two-dimensional Rashba ferromagnets. *Phys. Rev. B* **92**, 014402 (2015).
- [11] Liu, L. *et al.* Spin-torque switching with the giant spin Hall effect of tantalum. *Science* **336**, 555–558 (2012).
- [12] Demidov, V. E. *et al.* Magnetic nano-oscillator driven by pure spin current. *Nat. Mater.* **11**, 1028–1031 (2012).
- [13] Kampfrath, T. *et al.* Terahertz spin current pulses controlled by magnetic heterostructures. *Nat. Nanotechnol.* **8**, 256–260 (2013).
- [14] Borders, W. A. *et al.* Analogue spin-orbit torque device for artificial-neural-network-based associative memory operation. *Appl. Phys. Express* **10**, 013007 (2016).
- [15] Brataas, A., Nazarov, Y. V. & Bauer, G. E. Finite-element theory of transport in ferromagnet-normal metal systems. *Phys. Rev. Lett.* **84**, 2481 (2000).

- [16] Tserkovnyak, Y., Brataas, A., Bauer, G. E. & Halperin, B. I. Nonlocal magnetization dynamics in ferromagnetic heterostructures. *Rev. Mod. Phys.* **77**, 1375 (2005).
- [17] Wang, H., Du, C., Hammel, P. C. & Yang, F. Antiferromagnonic spin transport from $\text{Y}_3\text{Fe}_5\text{O}_{12}$ into NiO. *Phys. Rev. Lett.* **113**, 097202 (2014).
- [18] Wang, H. *et al.* Spin-orbit-torque switching mediated by an antiferromagnetic insulator. *Phys. Rev. Appl.* **11**, 044070 (2019).
- [19] Cui, B. *et al.* Field-free spin-orbit torque switching of perpendicular magnetization by the Rashba interface. *ACS Appl. Mater. Interfaces* **11**, 39369–39375 (2019).
- [20] Lin, W., Chen, K., Zhang, S. & Chien, C. L. Enhancement of thermally injected spin current through an antiferromagnetic insulator. *Phys. Rev. Lett.* **116**, 186601 (2016).
- [21] Moriyama, T. *et al.* Anti-damping spin transfer torque through epitaxial nickel oxide. *Appl. Phys. Lett.* **106**, 162406 (2015).
- [22] Li, S., Zhao, X., Liu, W., Zhao, X. & Zhang, Z. Modulation of spin-orbit torque induced magnetization switching in Pt/CoFe through oxide interlayers. *Appl. Phys. Lett.* **114**, 212404 (2019).
- [23] Şahin, C. & Flatté, M. E. Tunable giant spin Hall conductivities in a strong spin-orbit semimetal: $\text{Bi}_{1-x}\text{Sb}_x$. *Phys. Rev. Lett.* **114**, 107201 (2015).
- [24] Liu, L., Moriyama, T., Ralph, D. & Buhrman, R. Spin-torque ferromagnetic resonance induced by the spin Hall effect. *Phys. Rev. Lett.* **106**, 036601 (2011).
- [25] Fang, D. *et al.* Spin-orbit-driven ferromagnetic resonance. *Nat. Nanotechnol.* **6**, 413–417 (2011).
- [26] Gao, T. *et al.* Intrinsic spin-orbit torque arising from the Berry curvature in a metallic-magnet/Cu-oxide interface. *Phys. Rev. Lett.* **121**, 017202 (2018).
- [27] Gao, T. & Ando, K. Spin-orbit torques. *Handbook of Magnetic Materials*, vol. 29, chap. 1, 1–55 (Elsevier, 2020).
- [28] Pai, C.-F., Ou, Y., Vilela-Leão, L. H., Ralph, D. C. & Buhrman, R. A. Dependence of the efficiency of spin Hall torque on the transparency of Pt/ferromagnetic layer interfaces. *Phys. Rev. B* **92**, 064426 (2015).
- [29] Kim, Y. S. *et al.* Thickness-dependent bulk properties and weak antilocalization effect in topological insulator Bi_2Se_3 . *Phys. Rev. B* **84**, 073109 (2011).
- [30] Fritzsche, H. Electrical properties of germanium semiconductors at low temperatures. *Phys.*

- Rev.* **99**, 406 (1955).
- [31] Gao, B., Gehring, P., Burghard, M. & Kern, K. Gate-controlled linear magnetoresistance in thin Bi₂Se₃ sheets. *Appl. Phys. Lett.* **100**, 212402 (2012).
 - [32] Haney, P. M., Lee, H.-W., Lee, K.-J., Manchon, A. & Stiles, M. Current induced torques and interfacial spin-orbit coupling: Semiclassical modeling. *Phys. Rev. B* **87**, 174411 (2013).
 - [33] Nguyen, M.-H., Ralph, D. C. & Buhrman, R. A. Spin torque study of the spin Hall conductivity and spin diffusion length in platinum thin films with varying resistivity. *Phys. Rev. Lett.* **116**, 126601 (2016).
 - [34] Allen, G., Manipatruni, S., Nikonov, D. E., Doczy, M. & Young, I. A. Experimental demonstration of the coexistence of spin Hall and Rashba effects in β - tantalum/ferromagnet bilayers. *Phys. Rev. B* **91**, 144412 (2015).
 - [35] Wang, T.-C., Chen, T.-Y., Wu, C.-T., Yen, H.-W. & Pai, C.-F. Comparative study on spin-orbit torque efficiencies from W/ferromagnetic and W/ferrimagnetic heterostructures. *Phys. Rev. Mater.* **2**, 014403 (2018).
 - [36] Zhu, L., Ralph, D. C. & Buhrman, R. A. Effective spin-mixing conductance of heavy-metal–ferromagnet interfaces. *Phys. Rev. Lett.* **123**, 057203 (2019).
 - [37] Zwierzycki, M., Tserkovnyak, Y., Kelly, P. J., Brataas, A. & Bauer, G. E. W. First-principles study of magnetization relaxation enhancement and spin transfer in thin magnetic films. *Phys. Rev. B* **71**, 064420 (2005).
 - [38] Shen, K., Wang, L. & Xia, K. Breakdown of the Sharvin limit in spin pumping with interfacial Rashba spin-orbit coupling. *Phys. Rev. B* **99**, 045421 (2019).
 - [39] Fischer, G., Hoffmann, H. & Vancea, J. Mean free path and density of conductance electrons in platinum determined by the size effect in extremely thin films. *Phys. Rev. B* **22**, 6065 (1980).
 - [40] Saito, S. & Maeda, T. Work function of ferromagnetic metals and alloys. *Vacuum (Japan)* **24**, 220–222 (1981).
 - [41] Xia, K., Kelly, P. J., Bauer, G., Brataas, A. & Turek, I. Spin torques in ferromagnetic/normal-metal structures. *Phys. Rev. B* **65**, 220401 (2002).
 - [42] Zimmler, M. A. *et al.* Current-induced effective magnetic fields in Co/Cu/Co nanopillars. *Phys. Rev. B* **70**, 184438 (2004).
 - [43] Bauer, G. E. *et al.* Spin accumulation and decay in magnetic Schottky barriers. *Phys. Rev.*

- B* **72**, 155304 (2005).
- [44] Brataas, A., Kent, A. D. & Ohno, H. Current-induced torques in magnetic materials. *Nat. Mater.* **11**, 372–381 (2012).
 - [45] Dubowik, J. *et al.* Non-negligible imaginary part of the spin-mixing conductance and its impact on magnetization dynamics in heavy-metal–ferromagnet bilayers. *Phys. Rev. Applied* **13**, 054011 (2020).
 - [46] Xu, J., Wang, E., Ting, C. & Su, W. Tight-binding theory of the electronic structures for rhombohedral semimetals. *Phys. Rev. B* **48**, 17271 (1993).
 - [47] Tserkovnyak, Y., Brataas, A. & Bauer, G. E. W. Enhanced Gilbert damping in thin ferromagnetic films. *Phys. Rev. Lett.* **88**, 117601 (2002).
 - [48] Tserkovnyak, Y., Brataas, A. & Bauer, G. E. W. Spin pumping and magnetization dynamics in metallic multilayers. *Phys. Rev. B* **66**, 224403 (2002).
 - [49] Cogulu, E. *et al.* Quantifying spin-orbit torques in antiferromagnet–heavy-metal heterostructures. *Phys. Rev. Lett.* **128**, 247204 (2022).
 - [50] Yang, H., Chen, H., Tang, M., Hu, S. & Qiu, X. Characterization of spin-orbit torque and thermoelectric effects via coherent magnetization rotation. *Phys. Rev. B* **102**, 024427 (2020).
 - [51] Lee, J. W., Park, J. Y., Yuk, J. M. & Park, B.-G. Spin-orbit torque in a perpendicularly magnetized ferrimagnetic Tb-Co single layer. *Phys. Rev. Applied* **13**, 044030 (2020).
 - [52] Mishra, R. *et al.* Anomalous current-induced spin torques in ferrimagnets near compensation. *Phys. Rev. Lett.* **118**, 167201 (2017).
 - [53] Finley, J. & Liu, L. Spin-orbit-torque efficiency in compensated ferrimagnetic cobalt-terbium alloys. *Phys. Rev. Applied* **6**, 054001 (2016).
 - [54] Zhu, L., Ralph, D. C. & Buhrman, R. A. Highly efficient spin-current generation by the spin Hall effect in $\text{Au}_{1-x}\text{Pt}_x$. *Phys. Rev. Applied* **10**, 031001 (2018).
 - [55] Chi, Z. *et al.* The spin Hall effect of Bi-Sb alloys driven by thermally excited Dirac-like electrons. *Sci. Adv.* **6**, eaay2324 (2020).
 - [56] Deorani, P. *et al.* Observation of inverse spin Hall effect in bismuth selenide. *Phys. Rev. B* **90**, 094403 (2014).
 - [57] Wang, Y. *et al.* Topological surface states originated spin-orbit torques in Bi_2Se_3 . *Phys. Rev. Lett.* **114**, 257202 (2015).
 - [58] Tung, R. T. Electron transport of inhomogeneous Schottky barriers. *Appl. Phys. Lett.* **58**,

- 2821–2823 (1991).
- [59] Zhang, W., Han, W., Jiang, X., Yang, S.-H. & SP Parkin, S. Role of transparency of platinum–ferromagnet interfaces in determining the intrinsic magnitude of the spin Hall effect. *Nat. Phys.* **11**, 496–502 (2015).
 - [60] Baumgartner, M. *et al.* Spatially and time-resolved magnetization dynamics driven by spin–orbit torques. *Nat. Nanotechnol.* **12**, 980–986 (2017).
 - [61] Lee, J. M. *et al.* Oscillatory spin-orbit torque switching induced by field-like torques. *Commun. Phys.* **1**, 1–7 (2018).
 - [62] Vlasov, S. M., Kwiatkowski, G. J., Lobanov, I. S., Uzdin, V. M. & Bessarab, P. F. Optimal protocol for spin-orbit torque switching of a perpendicular nanomagnet. *Phys. Rev. B* **105**, 134404 (2022).
 - [63] Yan, B. & Felser, C. Topological materials: Weyl semimetals. *Annu. Rev. Condens. Matter Phys.* **8**, 337–354 (2017).
 - [64] Lv, B. Q., Qian, T. & Ding, H. Experimental perspective on three-dimensional topological semimetals. *Rev. Mod. Phys.* **93**, 025002 (2021).
 - [65] Deng, Y. *et al.* Gate-tunable room-temperature ferromagnetism in two-dimensional Fe_3GeTe_2 . *Nature* **563**, 94–99 (2018).
 - [66] Tang, M. *et al.* Continuous manipulation of magnetic anisotropy in a van der Waals ferromagnet via electrical gating. *Nat. Electron.* **6**, 28–36 (2023).

Acknowledgements

This work was supported by JSPS KAKENHI (Grant Numbers 22H04964, 19H00864, 20H00337, 20H02593), the JST FOREST Program (Grant Number JPMJFR2032), the Canon Foundation, the Asahi Glass Foundation, the JGC-S Scholarship Foundation, the Spintronics Research Network of Japan (Spin-RNJ), and MEXT Initiative to Establish Next-generation Novel Integrated Circuits Centers (X-NICS) (Grant Number: JPJ011438). T.G. acknowledge the financial support by JSPS KAKENHI (Grant Number 22K14561). A.Q., R.E.T., and A.B. were supported by the Research Council of Norway through its Centres of Excellence funding scheme, Project No. 262633, “QuSpin”. A.Q. was supported by the Norwegian Financial Mechanism Project No. 2019/34/H/ST3/00515, “2Dtronics”.

Author contributions

T.G., S.Z., and H.N. fabricated devices. T.G., and S.H. collected and analysed the data with the help of Y.T., and A.A., H.A., and R.T. performed structural characterizations. K.A. and T.G. designed the experiments and developed the explanation. A.Q., R.E.T., and A.B. performed the theoretical calculations and developed the explanation of the experimental results. T.G. and K.A. wrote the manuscript with the help of A.Q., R.E.T., and A.B. All authors discussed the results and reviewed the manuscript.

Competing interests

The authors declare no competing interests.

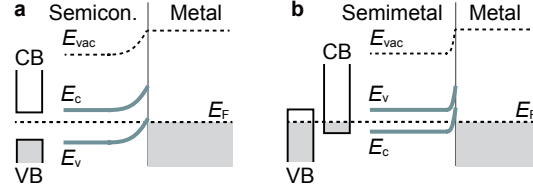


Figure 1. Energy barrier for charge transport across interfaces. Illustration of energy band diagrams for **a**, metal/semiconductor, and **b**, metal/semimetal contacts in thermal equilibrium. When electrons are transferred from the semiconductor or the semimetal to the metal upon equilibration of the Fermi levels E_F , the semiconductor or semimetal conduction band (CB) edge E_c and valence band (VB) edge E_v will bend upwards, leading to the creation of a depletion region. E_{vac} represents the vacuum level.

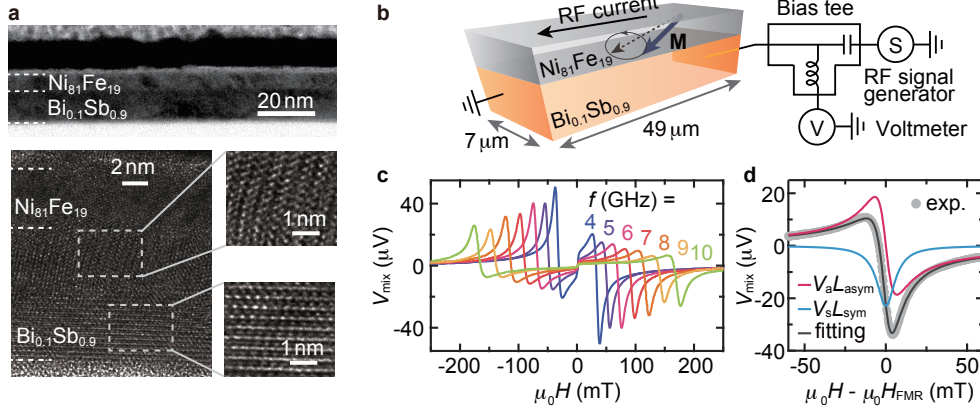


Figure 2. Structural characterization and ST-FMR. **a**, Bright-field cross-sectional TEM image (upper panel) and corresponding high-resolution image (bottom left panel) of the $\text{Ni}_{81}\text{Fe}_{19}$ (6 nm)/ $\text{Bi}_{0.1}\text{Sb}_{0.9}$ (10 nm) bilayer. The bottom right panel shows enlarged images of the selected regions indicated by the white dashed rectangles in the $\text{Bi}_{0.1}\text{Sb}_{0.9}$ layer. **b**, Schematic of the ST-FMR measurement on the in-plane magnetized $\text{Ni}_{81}\text{Fe}_{19}$ / $\text{Bi}_{0.1}\text{Sb}_{0.9}$ bilayer. The applied RF current induces effective fields, which drive precession of the magnetization \mathbf{M} around the external magnetic field \mathbf{H} (dashed arrow), where \mathbf{H} is applied at 45° with respect to the longitudinal direction of the device. **c**, Magnetic field H dependence of the rectified voltage V_{mix} for the $\text{Ni}_{81}\text{Fe}_{19}$ (6 nm)/ $\text{Bi}_{0.1}\text{Sb}_{0.9}$ (10 nm) bilayer measured at room temperature with RF current frequencies of 4-10 GHz. **d**, Fitting result of the ST-FMR signal for the sample used in (c) at 7 GHz. The turquoise and red curves present the symmetric Lorentzian ($V_s L_{\text{sym}}$) and antisymmetric Lorentzian ($V_a L_{\text{asym}}$) components, respectively.

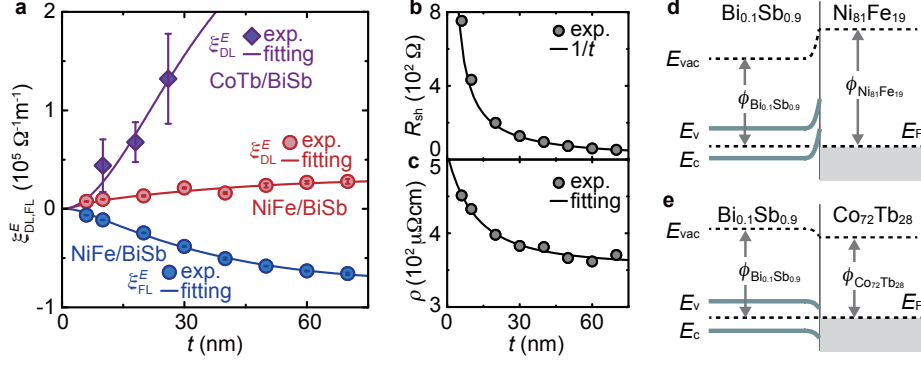


Figure 3. Characterization of SOTs and transport properties. **a**, DL(FL) SOT efficiency per electric field $\xi_{\text{DL(FL)}}^E$ as a function of the $\text{Bi}_{0.1}\text{Sb}_{0.9}$ layer thickness t for the $\text{Ni}_{81}\text{Fe}_{19}(6 \text{ nm})/\text{Bi}_{0.1}\text{Sb}_{0.9}$ and $\text{Co}_{72}\text{Tb}_{28}(6 \text{ nm})/\text{Bi}_{0.1}\text{Sb}_{0.9}$ bilayers. The error bars correspond to the standard deviation from the ST-FMR measurements in multiple devices and the linear fit to the second harmonic signals. The solid curves are fits to the ξ_{DL}^E and ξ_{FL}^E data obtained by employing the drift-diffusion approach given as equations (1) and (2). Thickness t dependence of **b**, sheet resistance R_{sh} , and **c**, corresponding 3D resistivity ρ for the $\text{Bi}_{0.1}\text{Sb}_{0.9}$ film. All measurements were performed at room temperature. Simplified energy band diagrams of the **d**, $\text{Ni}_{81}\text{Fe}_{19}/\text{Bi}_{0.1}\text{Sb}_{0.9}$, and **e**, $\text{Co}_{72}\text{Tb}_{28}/\text{Bi}_{0.1}\text{Sb}_{0.9}$ bilayers in thermal equilibrium. At the $\text{Ni}_{81}\text{Fe}_{19}/\text{Bi}_{0.1}\text{Sb}_{0.9}$ interface, electron transfer from $\text{Bi}_{0.1}\text{Sb}_{0.9}$ to $\text{Ni}_{81}\text{Fe}_{19}$ occurs to equilibrate the Fermi levels, as the work function $\phi_{\text{Ni}_{81}\text{Fe}_{19}} > \phi_{\text{Bi}_{0.1}\text{Sb}_{0.9}}$. This results in the creation of an electron depletion region at the atomic scale on the $\text{Bi}_{0.1}\text{Sb}_{0.9}$ side. In contrast, at the $\text{Co}_{72}\text{Tb}_{28}/\text{Bi}_{0.1}\text{Sb}_{0.9}$ interface, the difference in the work functions gives rise to transfer of electrons from $\text{Co}_{72}\text{Tb}_{28}$ to $\text{Bi}_{0.1}\text{Sb}_{0.9}$ because $\phi_{\text{Co}_{72}\text{Tb}_{28}} < \phi_{\text{Bi}_{0.1}\text{Sb}_{0.9}}$, and thus, nearly no electron barrier is formed on the $\text{Bi}_{0.1}\text{Sb}_{0.9}$ side.

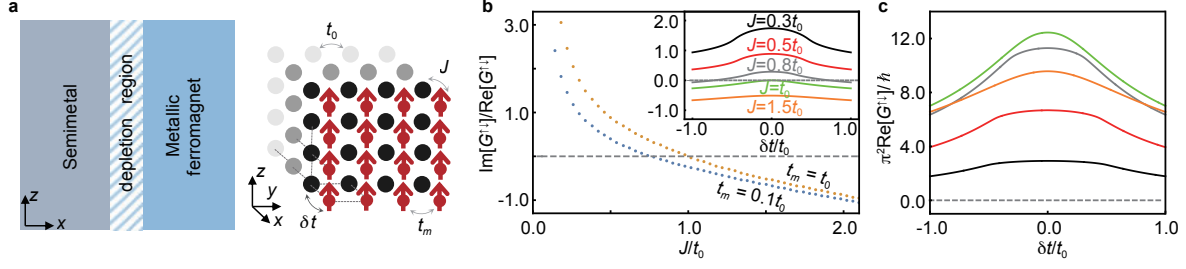


Figure 4. Theoretical modelling. **a**, (Left) Schematic setup of the semimetal/ferromagnetic-metal heterostructure and induced depletion region at the interface. (Right) Semi-infinite 3D cubic lattice structure and its relevant parameters used for the tight-binding model. The ferromagnetic metal is modelled by a 2D layer as a boundary condition with a hopping integral t_m , while the semimetal layer is modelled by a semi-infinite region with a hopping integral t_0 , and J is the exchange coupling between the spin of conduction electrons in the semimetal layer and magnetic moments in the ferromagnetic layer. J and $\delta t = t_0 - t_m$ effectively represent spin-dependent and spin-independent hopping across an energy barrier induced by the depletion region. **b**, Ratio between the imaginary and real parts of the spin mixing conductance $G^{\uparrow\downarrow}$ as a function of spin-independent interfacial hopping amplitude δt and spin-dependent interfacial hopping amplitude J . **c**, Real part of the spin mixing conductance $\text{Re}[G^{\uparrow\downarrow}]$ as a function of δt for various J .

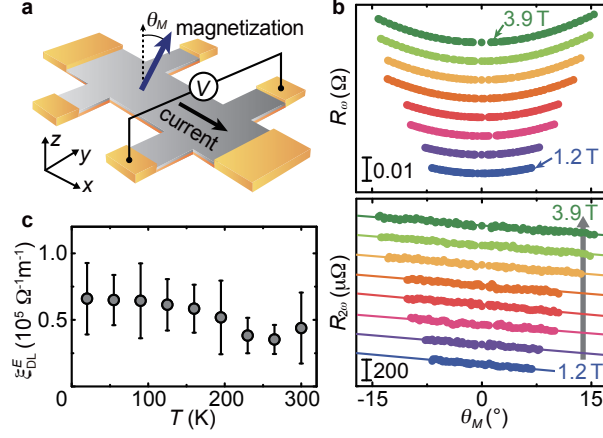


Figure 5. Harmonic signals and temperature dependence of SOT. **a**, Schematic of the out-of-plane angular-dependent harmonic Hall measurement on the perpendicularly magnetized $\text{Co}_{72}\text{Tb}_{28}/\text{Bi}_{0.1}\text{Sb}_{0.9}$ bilayer. An alternating current is applied along the longitudinal direction of the device with an external magnetic field H rotating in the xz plane, where the magnetization coherently rotates with H . The magnetization angle θ_M represents the angle between the net magnetization and film normal directions. **b**, First R_ω and second $R_{2\omega}$ harmonic signals as a function of the magnetization angle θ_M for the $\text{Co}_{72}\text{Tb}_{28}(6 \text{ nm})/\text{Bi}_{0.1}\text{Sb}_{0.9}(10 \text{ nm})$ bilayer at room temperature. The signals were recorded simultaneously under different external magnetic fields, 1.2 to 3.9 T. **c**, DL torque efficiency per electric field ξ_{DL}^E as a function of temperature T for the $\text{Co}_{72}\text{Tb}_{28}(6 \text{ nm})/\text{Bi}_{0.1}\text{Sb}_{0.9}(10 \text{ nm})$ bilayer. The error bars denote the standard deviation from the linear fit to the second harmonic signals.